AGU ADVANCING EARTH AND SPACE SCIENCES

Geophysical Research Letters

RESEARCH LETTER
10.1029/2026GL122025

Spatial Heterogeneity and Inhomogeneity of Cirrus Microphysical Properties on Kilometer Spatial Scales

John D'Alessandro[1], **Odran Sourdeval**[1], and **Martina Krämer**[2,3]

[1]Université de Lille, CNRS, UMR 8518 - LOA - Laboratoire d'Optique Atmosphérique, Lille, France, [2]Now at Institute for Physics of the Atmosphere (IPA), Johannes Gutenberg University, Mainz, Germany, [3]Institute of Climate and Energy Systems (ICE-4), Research Center, Jülich, Jülich, Germany

Key Points:

- The spatial heterogeneity and inhomogeneity of cirrus properties is evaluated using ~60 hr of in situ measurements acquired globally
- The spatial heterogeneity of ice number concentration and mass content increases for increasingly thin/tenuous cirrus
- Localized absences of small ice are a primary feature of cirrus inhomogeneity/heterogeneity, and is ubiquitous in cirrus clouds globally

Supporting Information:

Supporting Information may be found in the online version of this article.

Correspondence to:

J. D'Alessandro,
john.d-alessandro@univ-lille.fr

Citation:

D'Alessandro, J., Sourdeval, O., & Krämer, M. (2026). Spatial heterogeneity and inhomogeneity of cirrus microphysical properties on kilometer spatial scales. *Geophysical Research Letters*, *53*, e2026GL122025. https://doi.org/10.1029/2026GL122025

Received 27 JAN 2026
Accepted 18 MAY 2026

Author Contributions:

Conceptualization: John D'Alessandro
Formal analysis: John D'Alessandro
Investigation: John D'Alessandro
Methodology: John D'Alessandro
Writing – original draft: John D'Alessandro

Abstract Previous studies reporting the spatial inhomogeneity and heterogeneity of cirrus cloud properties have primarily been case studies derived from relatively small data sets. This study evaluates the spatial heterogeneity and inhomogeneity of cirrus bulk microphysical properties using ~60 hr of in situ measurements from eight field campaigns. The spatial heterogeneity of ice concentration (ice water content) increases with decreasing ice concentration (ice water content), revealing more tenuous cirrus are more spatially heterogenous. Cirrus clouds often contain heavily skewed distributions of ice concentrations, which also possess high spatial heterogeneity. This is primarily due to the absence of small ice crystals (diameter < ~50 μm) within localized regions of the clouds. These regions contain lower ozone concentrations and broader distributions of relative humidity with respect to ice. The greater variation of relative humidity suggests enhanced temperature perturbations resulting in greater frequencies of subsaturated samples, which preferentially sublimate small ice (e.g., via the kelvin effect).

Plain Language Summary The heterogeneity/inhomogeneity of cirrus bulk microphysical properties has been linked with increased satellite retrieval error, and has also been shown to provide information on the evolutionary pathways of cirrus clouds (e.g., perturbations resulting from wave activity). This study uses ~60 hr of airborne, in situ measurements acquired globally to provide a high precision evaluation of cirrus spatial heterogeneity/inhomogeneity on the scale of kilometers. A strong, negative relationship is found between ice content and spatial heterogeneity, where increasingly tenuous clouds generally possess more spatially heterogeneous ice water content and ice number concentrations. A common pattern of inhomogeneity is also observed in cirrus globally, where cirrus clouds commonly have localized absences of small ice crystals within them. Future research is encouraged for diagnosing what conditions lead to increased spatial heterogeneity/inhomogeneity of cirrus clouds, as well as the ubiquitous absence of small ice. Such findings are crucial as ever-increasing spatial resolutions of models ultimately result in increasing representativeness of underlying, small-scale cirrus processes/features.

1. Introduction

The spatial inhomogeneity and heterogeneity (often used interchangeably) of bulk microphysical properties of cirrus clouds on kilometer spatial scales has been largely uncharacterized beyond select case studies/regional data sets. Many of these studies evaluating the spatial heterogeneity/inhomogeneity of cirrus clouds often evaluate macro-scale features such as optical thickness or cloud fraction (e.g., Schäfer et al., 2017; Wolters et al., 2010). Evaluating inhomogeneity/heterogeneity can also provide insight into cirrus formation/evolution processes. For example, greater inhomogeneity can be indicative of increased gravity wave activity (e.g., Podglajen et al., 2018). Further, incorporating the heterogeneity of cirrus properties into climate models has been shown to improve predictive output (e.g., Gu & Liou, 2006). Aside from these physical insights, it is important to consider the spatial heterogeneity of cirrus properties due to their potential for introducing biases into spaceborne remote sensing retrievals. Previous studies have evaluated this bias by simulating cloud fields and their spatial heterogeneity (e.g., Fauchez et al., 2015, 2018; Zhuravleva & Nasrtdinov, 2021), where Fauchez et al. (2015) found that such biases are most significant for optically thick clouds.

The purpose of this study is to inform the research community of the observed horizontal spatial inhomogeneity/heterogeneity of different bulk microphysical properties within cirrus clouds by pulling from ~60 hr of in situ measurements acquired globally. Section 2 provides an overview of the data sets used in this study. Section 3 introduces parameters used to characterize inhomogeneity and heterogeneity, and how both properties are defined in this study. Section 4 provides findings and Section 5 includes additional discussion. Section 6 offers concluding remarks.

2. In Situ Measurements

Cloud microphysical data is from Krämer et al. (2025a), who constructed particle size distribution (PSD) data from in situ measurements acquired during eleven field campaigns. Only eight field campaigns meet our data conditions described below, which include the Airborne Tropical Tropopause Experiment (ATTREX; Jensen et al., 2017), the Midlatitude experiment (ML-CIRRUS; Voigt et al., 2017), Aerosol, Cloud, Precipitation, and Radiation Interaction and Dynamics of CONvective Cloud Systems (ACRIDICON; Wendisch et al., 2016), the Convective Transport of Active Species in the Tropics (CONTRAST; Pan et al., 2017), Pacific Oxidants, Sulfur, Ice, Dehydration, and cONvection (POSIDON; Krämer et al., 2020a, 2020b), Stratosphere-Troposphere Analyses of Regional Transport (START08; Pan et al., 2010) and Stratospheric and upper tropospheric processes for better climate predictions (STRATOCLIM; Krämer et al., 2020a, 2020b) campaigns. Sample size statistics from the field campaigns are in Figure S1 in Supporting Information S1.

PSD data is obtained from combining single scattering probe and optical array probe measurements. These instruments include a Cloud and Aerosol Spectrometer (CAS), Cloud Imaging Probe (CIP), Cloud Droplet Probe (CDP), Fast Cloud Droplet probe (FCDP), Two-Dimensional Cloud probe (2DC) and Two-dimensional Stereo probe (2DS). PSDs include particles having diameters from 3 to 1,000 μm. The 1 Hz ice concentrations ($N_{1\text{Hz}}$) are obtained from PSD data, and ice water content ($\text{IWC}_{1\text{Hz}}$) is derived from m–D relationships following Krämer et al. (2016). In-cloud samples are those with $\text{IWC}_{1\text{Hz}} > 10^{-5}$ g m^{-3}. This study only examines measurements where there are 15 consecutive in-cloud seconds along the flight path (∼1.5–3.5 km), which are defined as transects. Parameters such as transect average ice concentration (N) and ice water content (IWC) are determined from averaging 1 Hz PSDs within the respective transects. Parameters referring to 1 Hz samples contain the "1 Hz" subscript. Some results will be presented in the context of in-cloud flight legs, defined as three or more neighboring transects (illustrated in Section 3). Note that transects are split up into 15 sample intervals; whereas in-cloud flight legs are never split up, and the number of neighboring transects can far exceed three. Further instrumentation details are provided in Krämer et al. (2020a, 2020b, 2025a), including measurements of temperature, relative humidity with respect to ice (RHi) and ozone concentration (O_3) used in this study.

The data analysis is restricted to temperatures below −38°C to ensure ice clouds are sampled. Additionally, a simple condition to limit the inclusion of precipitating ice is applied: all samples must have RHi > 50%. This condition is chosen based on Figure S2, which includes further discussion in Supporting Information S1.

3. Heterogeneity and Inhomogeneity Metrics

We first provide very general definitions of spatial inhomogeneity and heterogeneity for the purposes of this study: inhomogeneity concerns broad changes in the magnitudes of a property within a given space, whereas heterogeneity only considers localized changes within a space at relatively smaller spatial scales. To quantify spatial inhomogeneity and heterogeneity of cirrus properties, we compute these properties for transects (discretized regions of in cloud in situ measurements; Section 2). An intuitive approach to determine 1-D heterogeneity (H) is expressed as

$$H = \sum_{m=2}^{T} |X(m) - X(m-1)| \tag{1}$$

where X is any given variable (e.g., IWC), m is the placeholder for the sample's location within the transect and T is the number of samples within a transect ($T = 15$). Note that H increases with greater absolute differences between neighboring samples. An illustration of this is provided further below.

To produce a normalized expression of heterogeneity, a maximum and minimum value of H must be obtained. The minimum value can be expressed as

$$H_{\min} = \sum_{m=2}^{T} X_{\mathrm{sort}}(m) - X_{\mathrm{sort}}(m-1) \tag{2}$$

where X_{sort} is the variable of the transect samples sorted with ascending values. To obtain the maximum H, H should be solved for all possible permutations (i) of X shuffled within a given transect. Namely,

$$H_{\max} = \max_{i=1,2,\ldots,1{,}000{,}000}(H_{\mathrm{perm},i}) \tag{3}$$

where

$$H_{\mathrm{perm}} = \sum_{m=2}^{T} |X_{\mathrm{perm}}(m) - X_{\mathrm{perm}}(m-1)| \tag{4}$$

and X_{perm} is a given variable of the randomly shuffled transect samples. Note that only a maximum of 1,000,000 possible permutations are computed.

We combine these terms to produce a normalized heterogeneity equation

$$\mathrm{Het} = \frac{H - H_{\min}}{H_{\max} - H_{\min}}. \tag{5}$$

This normalization equation is ∼0 for spatially homogeneous transects and approaches 1 for spatially heterogeneous transects. Note that the inclusion of $H_{\min}$ into Equation 5 broadly distinguishes between heterogeneity from inhomogeneity as previously defined. Namely, subtracting $H_{\max}$ by $H_{\min}$ removes consideration of net differences over longer length scales, only diagnosing variability on relatively smaller scales. Following this, an expression for inhomogeneity as a combination of the net differences over longer and shorter length scales can be intuited from Equation 5 as

$$\mathrm{Inh} = \frac{H}{H_{\max}}. \tag{6}$$

where consecutive increasing or decreasing samples contribute to the net variability of the transect. H is still weighted by $H_{\max}$ to weight transects with low and high average X, since those with high X will consequently produce greater H (not shown). In this study, we evaluate the heterogeneity and inhomogeneity of $N_{1\mathrm{Hz}}$ and $\mathrm{IWC}_{1\mathrm{Hz}}$.

Figure 1a provides an idealized visualization of spatial homogeneity, inhomogeneity and heterogeneity of an arbitrary cloud property (X). Note that spatial inhomogeneity and heterogeneity are inherently different—in that spatially inhomogeneous transects can lack high spatial heterogeneity. This is illustrated in the three transects in Figure 1a: where the middle transect is inhomogeneous but not heterogeneous (Inh > 0 and Het ∼ 0), in contrast to the right transect which is both inhomogeneous and heterogeneous (Inh > 0 and Het > 0). Figures 1b and 1c show histograms of the heterogeneity of $\mathrm{IWC}_{1\mathrm{Hz}}$ ($\mathrm{Het}_{\mathrm{IWC}}$) and $N_{1\mathrm{Hz}}$ (Het_N) for different ranges of IWC and N, respectively. As IWC and N decrease, Het_N and $\mathrm{Het}_{\mathrm{IWC}}$ increase, respectively. This is suspected to result from more tenuous cirrus competing for available water vapor, in contrast to thicker cirrus likely of liquid origin (e.g., Krämer et al., 2020a, 2020b) having more abundant/accessible water vapor. This trend is similarly observed when interchanging Het_N and $\mathrm{Het}_{\mathrm{IWC}}$ with Inh_N and $\mathrm{Inh}_{\mathrm{IWC}}$, respectively (not shown). Further, this trend also appears to be scale invariant, as results are consistently observed for $T = 7$, 30, and 50 (not shown).

We also examine the skewness (τ) of the distributions of $\mathrm{IWC}_{1\mathrm{Hz}}$ and $N_{1\mathrm{Hz}}$ samples within each transect (τ_{IWC} and τ_N, respectively; discussed in Figure 1a). Skewness is used as a complementary indicator of inhomogeneity along with Inh. Due to the low sample size associated with transects (15), L-moments are used to derive more robust characterizations of skewness (Hosking, 1990). L-moments have been used in atmospheric research on topics ranging from regional climate to extreme precipitation events (e.g., Chen et al., 2023; Guttman et al., 1993). In

10.1029/2026GL122025

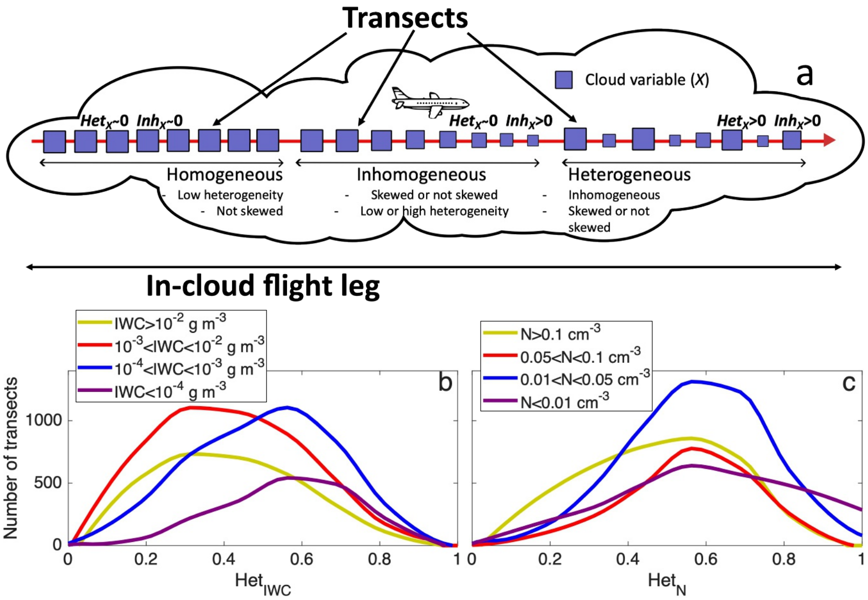

Figure 1. (a) Idealized diagram characterizing spatial homogeneity, inhomogeneity, and heterogeneity of an arbitrary cirrus property (X), including transect and in-cloud flight leg labels. Transects are regions of 15 neighboring 1 Hz in-cloud samples, and in-cloud flight legs are regions of three or more neighboring transects. Expected values of Het_X and Inh_X overlie the respective transects. (b) Histograms of Het_{IWC} for different ranges of IWC. (c) Histograms of Het_N for different ranges of N. Histograms in (b) and (c) are binned at 0.125 intervals.

contrast to conventional moments (power deviations from the mean), L-moments are determined from linear combinations of order statistics. τ is expressed as

$$\tau = \frac{L_3}{L_2}. \tag{7}$$

where L_3 and L_2 are the third and second L-moments expressed as

$$L_2 = 2\beta_1 + \beta_0. \tag{8}$$

$$L_3 = 6\beta_2 - 6\beta_1 + \beta_0. \tag{9}$$

$$\beta_1 = \frac{1}{T}\sum_{m=1}^{T}\left(\frac{m-1}{T-1}\right)X_{\text{sort}}(m) \tag{10}$$

$$\beta_2 = \frac{1}{T}\sum_{m=1}^{T}\frac{(m-1)(m-2)}{(T-1)(T-2)}X_{\text{sort}}(m) \tag{11}$$

and β_0 is the mean of X. In contrast to skewness derived from conventional moments, τ ranges from -1 to 1 for the left-most and right-most possible skewness, respectively.

A simple peak detection algorithm to diagnose the number of peaks in a transect (P) is also introduced to supplement the analysis, which are diagnosed at m where $X_{m-1} < X_m$ and $X_m > X_{m+1}$. Peaks are only determined for ice concentrations. They must exceed 0.5 of a logarithmically scaled ice crystal concentration [$\log_{10}(N_{1\text{Hz}})$], which corresponds to a factor of ~3–7 increase from the base of the peaks.

4. Results

Figures 2a–2c shows scatterplots of ice concentration skewness (τ_N) and N, and results are colored by Het_N (a), P (b), and τ_{IWC} (c). Datapoints are transects. Focusing on Figure 2a, almost none of the transects have values

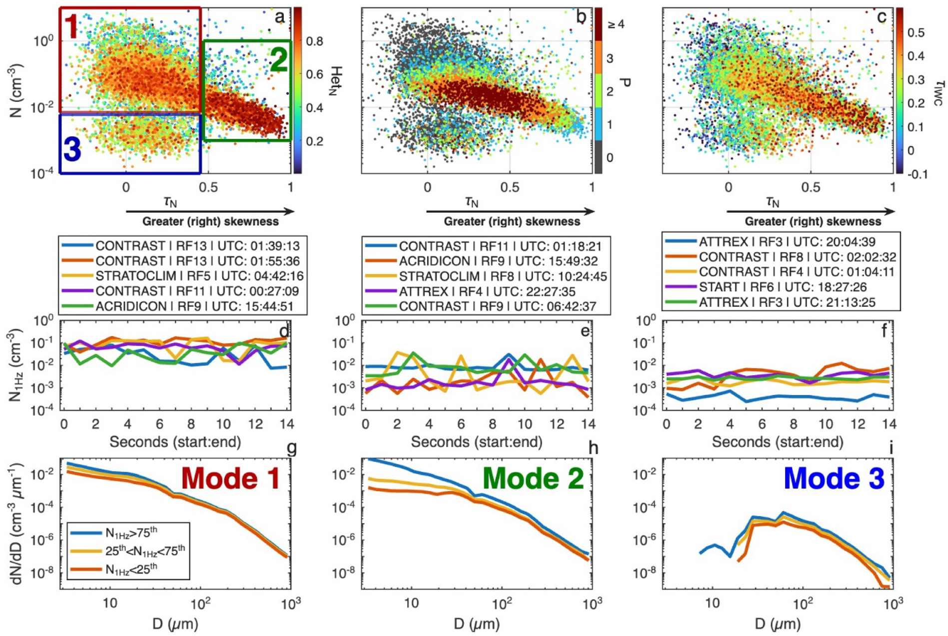

Figure 2. Ice concentration skewness (τ_N) and N scatterplots colored by spatial heterogeneity of ice concentration (Het_N; a), number of ice concentration peaks within the transect (P; b) and ice water content skewness (τ_{IWC}; c). Datapoints are transects. Boxes in (a) denote three modes (1, 2, 3) which are discussed in the text. Select transect time series are shown in panels (d)–(f) corresponding to Mode 1, 2, 3, respectively. Average PSDs are shown in panels (g)–(i) for all transects from Modes 1, 2, 3, respectively. The average PSDs are separately determined from 1 Hz PSDs where $N_{1\text{Hz}}$ exceeds the 75th percentiles (blue), within the 75th and 25th percentiles (yellow) and below the 25th percentiles (red) of the respective transects.

negatively skewed below −0.4, while there are numerous positively skewed values exceeding 0.5. Further, N tends to decrease with increasingly skewed transects. Additionally, Het_N generally increases with increasing skewness. We separate transects into three primary modes, which are denoted by the colored boxes in Figure 2a. Further discussion of these modes will continue later in this section, where Modes 1 and 3 which contain slightly positively/negatively skewed transects ($\tau_N < 0.45$) will be referred to as non-skewed transects, and Mode 2 containing heavily, positively skewed transects will be referred to as skewed transects ($\tau_N > 0.45$).

Scatterplots colored by P generally reveal a greater number of peaks for more positively skewed transects. However, the highest P occurs within $0.2 < \tau_N < 0.7$. Since this decrease in P at $\tau_N < 0.7$ is also where Het_N is greatest (Figure 2a), this highlights that greater heterogeneity is not associated with relatively large ranges/variances in the transects' N, since peaks must not exceed the 0.5 threshold. Finally, results are colored by $\text{IWC}_{1\text{HZ}}$ skewness (τ_{IWC}) to show that ice shattering on instrumentation inlets is not responsible for high τ_N. If it were, only τ_N would increase whereas τ_{IWC} should remain constant. However, τ_{IWC} similarly increases with increasing τ_N. Further, decreasing N with increasing τ_N is also inconsistent with ice shattering.

Our next objective is to separately evaluate transects from the three modes. To illustrate how ice concentrations are distributed within transects for these modes, panels 2d–f show select transect time series of $N_{1\text{Hz}}$ from Modes 1,2,3, respectively. Transects from Modes 1 (d) and 3 (f) show relatively constant $N_{1\text{Hz}}$ within the transects compared with $N_{1\text{Hz}}$ within transects from Mode 2 (e).

To compare how PSDs vary within the transects between the three Modes, Figures 2g–2i shows average PSDs for different $N_{1\text{Hz}}$ ranges within their respective transects. Specifically, $N_{1\text{Hz}}$ are separated as percentile ranges determined separately for their respective transects. The three PSDs are averaged from samples having $N_{1\text{Hz}} <$ 25th percentiles, 25th $< N_{1\text{Hz}} <$ 75th percentiles and $N_{1\text{Hz}} >$ 75th percentiles. For example, the $N_{1\text{Hz}} <$ 25th PSD (red line) is averaged from all $N_{1\text{Hz}}$ samples having ice concentrations in the bottom quartile of the respective transects. Focusing on panel 2g, the PSDs are relatively similar for the low skewed Mode 1. However, Mode 2 has larger differences in the overall PSD shapes, and these differences are only observed for ice crystals with diameters below ~40 μm (2h). This absence of small ice is most notable in Mode 3 (2i).

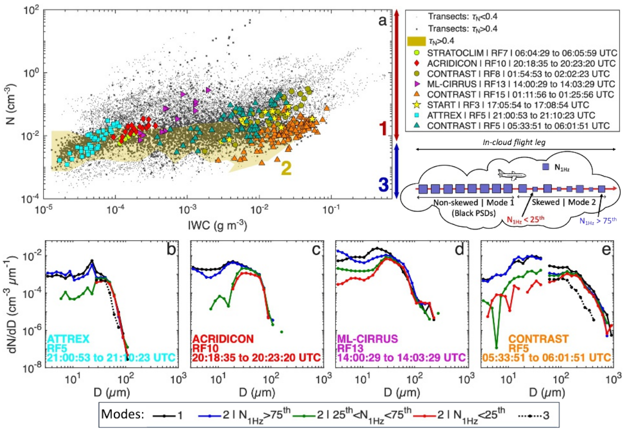

Figure 3. (a) Scatterplot of IWC and N. Datapoints are transects having $\tau_N < 0.45$ and x's are transects having $\tau_N > 0.45$. Gold shading corresponds to transects having $\tau_N > 0.45$, determined by applying $\tau_N = 0.45$ isopleths to a gridded IWC-N phase space (discussed further in text and SI). Large markers having identical colors and shapes correspond to select in-cloud flight legs. The 1, 2, 3 labels correspond to modes depicted in Figure 2a. Averaged PSDs for different in-cloud flight legs are shown in panels (b)–(e). PSDs are separately averaged for Mode 1 transects ($\tau_N < 0.45$ and $N > 0.008$ cm^{-3}) as black lines, Mode 2 ($\tau_N > 0.45$) for different percentile ranges of N_{1Hz} similar to Figures 2g–2I and Mode 3 ($\tau_N < 0.45$ and $N < 0.008$ cm^{-3}) as dotted lines. An idealized depiction of how transects and 1 Hz samples are selected for averaging PSDs is shown above panel (e).

Now we explore possible cause(s) resulting in skewed transects. For this, multiple in-cloud flight legs (i.e., sets of at least three consecutive, neighboring transects) will be examined as case studies to compare the neighboring skewed and non-skewed transects within the flight legs. This is done to (a) minimize possible environmental biases and (b) see whether cirrus clouds commonly contain transects from multiple modes. To explore the general microphysical characteristics of these in-cloud flight legs, Figure 3a shows a scatterplot of all transects in the IWC–N phase space (i.e., transect IWC related to N). Gray dots denote non-skewed transects ($\tau_N < 0.45$) whereas small gray x's denote skewed transects ($\tau_N > 0.45$). Corresponding to skewed transects in Figure 2a (Mode 2) is the yellow shaded region in Figure 3a. This region denotes isopleths at $\tau_N = 0.45$ mapped to a 2D convolution of τ_N in the IWC–N phase space. Red and blue double arrows next to the panel denote N ranges corresponding to Modes 1 and 3 in Figure 3a.

The assortment of large markers seen dispersed throughout the figure correspond to transects within select in-cloud flight legs (specified in the legend). The different marker colors and shapes correspond to the respective in-cloud flight legs.

All in-cloud flight legs shown contain transects with $\tau_N < 0.45$ (non-skewed) and $\tau_N > 0.45$ (skewed). They all generally have non-skewed transects possessing larger IWC and N relative to the skewed transects (excluding Mode 3). This is consistent with skewed transects within in-cloud flight legs being associated with reductions in ice content via processes such as the kelvin effect, wave activity, temperature perturbations, entrainment or sublimating ice. To explore this, Figures 3b–3e shows averaged transect PSDs within four of the in-cloud flight legs shown in panel a (colored text). The black PSDs are those averaged over all Mode 1 transects. The colored PSDs correspond to skewed transects' different N_{1Hz} percentile ranges relative to each transect, similar to Figures 2g–2i. The upper quartile (blue lines) corresponds to the highest N_{1Hz} and the lower quartile (red lines) corresponds to the lowest N_{1Hz} relative to each transect. An idealized diagram overlying panel e is provided for clarification.

All of the cases reveal trends consistent to those in Figures 2h and 2i where smaller ice crystals are absent in the skewed (Mode 2) and Mode 3 transects. They also show PSDs of Mode 1 transects generally containing either slightly higher or approximately similar PSDs compared with those of the upper quartile N_{1Hz} of skewed transects (blue lines). These cases combined with (a) the decreasing IWC and N toward skewed transect clusters within in-cloud flight legs (Figure 3a) and (b) decreasing N with increasing τ_N (Figures 2a–2c) highlight a ubiquitous absence of small ice particles within cirrus clouds.

The previous case studies demonstrate how this ice concentration inhomogeneity can occur localized within regions of cirrus clouds. Figure 4a further explores the statistics of localized small ice absence by showing the distribution of in-cloud flight legs' ratio of skewed transects (i.e., $\tau_N > 0.45$/all transects; green line), as well as the ratio of Modes 2&3 to all transects (purple line). For both distributions, approximately half of the in-cloud flight legs have ratios exceeding 0.2 (39% and 48% for Mode 2 and Mode 2&3 ratios, respectively). Figure 4b compliments Figure 2a by showing distributions of Het_N and Inh_N for transects from Modes 1,2,3. For the respective modes, Het_N and Inh_N distributions are quite similar to each other; both possess peaks in the distributions around ∼0.5–0.7 for non-skewed transects while skewed transects are shifted toward higher Het_N and Inh_N. Mode 2 has the most inhomogeneity and heterogeneity compared to the other two modes, likely because of localized small ice absences. This is in contrast to Mode 1 transects having abundant small ice and Mode 3 transects almost completely absent of small ice. Distributions of Inh_N are shifted to slightly larger values than their respective Het_N distributions, which is expected since Het_N minimizes the contribution of inhomogeneity (H_{min}) to its computation (Equation 5).

Figure 4c shows normalized frequency distributions of O_3 for the three modes, and 4d distributions similarly of RHi. Mode 1 and Modes 2&3 have notable differences in O_3, in that Mode 1 has notably higher O_3. This may be due to O_3 chemically reacting with prevailing ice nucleating particles and enhancing their nucleation tendencies,

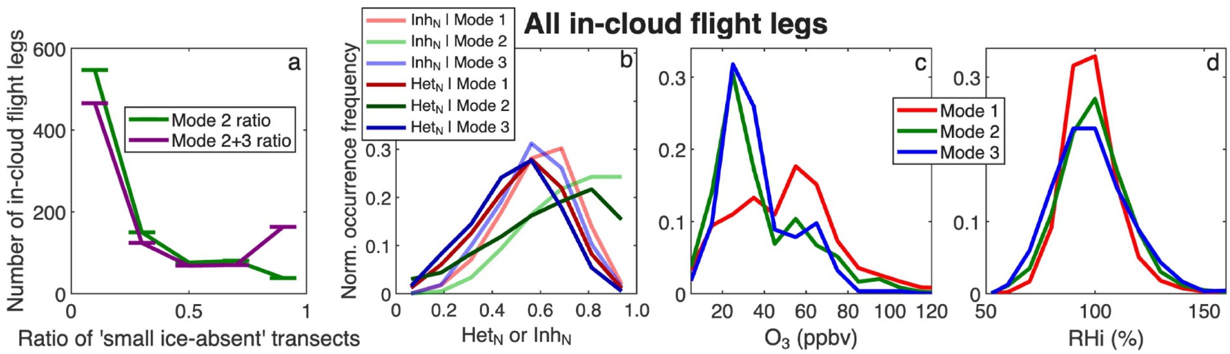

Figure 4. (a) The distribution of in-cloud flight legs' ratios of Mode 2 (green line) and Modes 2&3 (purple line) transects to all transects. (b) Distributions of Het_N (dark-shaded lines) and Inh_N (light-shaded lines) for Modes 1, 2, 3. (c) Distributions of O_3 and (d) RHi within the three Modes. All panels only include transects contained within in-cloud flight legs.

which has been previously reported for select species (e.g., Kanji et al., 2013; Zhang et al., 2020). This is consistent with relatively greater supersaturations for Modes 2&3, where ice is not effectively nucleating as for regions mixed with greater O_3 (4d). These and Het and Inh trends are also observed when only evaluating in-cloud flight legs containing Modes 1&2 (384 in-cloud flight legs; Figure S3 in Supporting Information S1), which minimizes environmental biases when comparing Modes 1&2. Further, we address the possible bias of small-ice absent transects being associated with virga: where these transects would be expected to occur at lower altitudes where ozone concentrations are lower. However, both the mean and median temperature of Modes 1&2 are within ±1°C, and are lowest (~8°C lower) for Mode 3, invalidating this possibility. Relatively low frequencies of Mode 2&3 transects are observed for midlatitude regions sampled during ML-CIRRUS, and relatively high frequencies are observed for tropical/subtropical regions sampled during ATTREX and CONTRAST (Figure S1 in Supporting Information S1), consistent with greater stratospheric mixing in the midlatitudes compared with the tropics (e.g., Holton et al., 1995; Liang et al., 2009). In contrast, the frequency of Mode 2&3 transects is relatively low for ACRIDICON and STRATOCLIM having sampled in the tropics and subtropics, respectively (Figure S1 in Supporting Information S1), which may suggest the importance of in situ photochemical production in these regions, which was noted during ACRIDICON (Wendisch et al., 2016).

5. Additional Discussion

Section 4 presented results evaluating and contrasting cirrus whose ice concentration distributions are skewed or not skewed. Although skewness is determine for linearly scaled N_{1Hz}, these modes are still observed when applied to a log-scaled N_{1Hz} [$\log_{10}(N_{1Hz})$; not shown]. Aside from O_3 trends, these inherent modes related to the absence of small ice are also consistent with the kelvin effect, characterized by the mass transfer of frozen condensate from smaller to larger particles due to differences in the saturation vapor pressure over curved surfaces. The increased number of subsaturated samples in Modes 2&3 (Figure 4d) may also suggest preferential sublimation of small ice via temperature perturbations/entrainment due their greater surface area to volume ratio). For example, modeling studies have shown this effect is expected in anvil cirrus and in the presence of gravity waves (Jensen et al., 2024), and gravity wave activity has been shown to be commonly unresolved and therefore underestimated in climate models (Atlas & Bretherton, 2023). The importance of continued exploration of cirrus inhomogeneity and small ice absence is further validated by the ubiquity of such characteristics. This is partly demonstrated by observed frequencies of Mode 2&3 transects amongst all field campaigns, where the ratio of Mode 2&3 transects ($\tau_N > 0.45$ or $N < 0.008$ cm^{-3}) to all transects ranges from 9% to 60% amongst the different campaigns (Figure S1 in Supporting Information S1).

To evaluate potential biases resulting from cirrus inhomogeneities impacting remote sensing retrievals, Figure S4 in Supporting Information S1 relates the volume optical extinction of neighboring Mode 1 and Mode 2 transects within in-cloud flight legs containing both Modes 1&2, finding that absolute differences commonly exceed an order of magnitude between the two modes (further discussed in SI). It is also increasingly important to consider small scale perturbations of cirrus properties given increasing model resolutions, ultimately warranting improved representativity of cirrus properties and underlying processes.

Potential uncertainty in the analysis may result from the inherent differences in sample volumes, and associated sampling statistics between the two sets of probes sampling small and large ice particles. Optical array probes have inherently larger sample volumes than spectrometers, meaning larger particles will have higher likelihoods of being sampled than smaller particles within the most tenuous cirrus. However, this bias is expected to be minimal due to computing statistics over long sampling durations, as well as by utilizing a relatively large data set for this study.

6. Conclusion

This study characterizes the spatial inhomogeneity and heterogeneity of cirrus bulk microphysical properties globally by evaluating ∼60 hr of in situ measurements acquired during eight field campaigns. Multiple parameters were used, including two novel metrics which diagnose the heterogeneity/inhomogeneity of regions having 15 consecutive in-cloud samples (i.e., transects; ∼1.5–3.5 km). Results show ice water content and ice concentration are negatively related to the spatial heterogeneity of ice water content and ice concentration, respectively.

Three primary modes of transects are found: (a) transects containing relatively high ice concentrations ($N > \sim 0.01\ \mathrm{cm}^{-3}$), (b) transects whose ice concentration distributions are skewed due to localized absences of small ice (which enhances the heterogeneity of ice concentrations) and (c) non-skewed transects exhibiting the greatest absence of small ice. While decreased ozone concentrations and broader distributions of relative humidity are associated with transects exhibiting the "absent small-ice" trend, future work should focus on addressing what atmospheric processes contribute to the increased heterogeneity/inhomogeneity and ubiquitous small ice absence.

Conflict of Interest

The authors declare no conflicts of interest relevant to this study.

Availability Statement

The in situ measurements are from the Cirrus Guide III in situ data set (Krämer et al., 2025b). All relevant processed data and code related to data processing/analysis is accessible at D'Alessandro (2026).

Acknowledgments
John D'Alessandro, Martina Krämer and Odran Sourdeval were supported by ANR and DFG (Grant ANR-23-CE01-0022) for project GLACIATE; Odran Sourdeval acknowledges support by the Simons Foundation (Grant SFI-MPS-SRM-00012102) and the Centre National d'Etudes Spatiales (CNES) through the EarthCARE and CIRSys3D projects.

References

Atlas, R., & Bretherton, C. S. (2023). Aircraft observations of gravity wave activity and turbulence in the tropical tropopause layer: Prevalence, influence on cirrus clouds, and comparison with global storm-resolving models. *Atmospheric Chemistry and Physics*, *23*(7), 4009–4030. https://doi.org/10.5194/acp-23-4009-2023

Chen, X., Zhu, D., Wang, M., & Liao, Y. (2023). Regional precipitation frequency analysis for 24-h duration using GPM and L-moments approach in South China. *Theoretical and Applied Climatology*, *152*(1), 709–722. https://doi.org/10.1007/s00704-023-04405-4

D'Alessandro, J. J. (2026). Datasets and scripts for cirrus heterogeneity transect data [Dataset]. https://doi.org/10.5281/zenodo.18390939

Fauchez, T., Dubuisson, P., Cornet, C., Szczap, F., Garnier, A., Pelon, J., & Meyer, K. (2015). Impacts of cloud heterogeneities on cirrus optical properties retrieved from space-based thermal infrared radiometry. *Atmospheric Measurement Techniques*, *8*(2), 633–647. https://doi.org/10.5194/amt-8-633-2015

Fauchez, T., Platnick, S., Sourdeval, O., Wang, C., Meyer, K., Cornet, C., & Szczap, F. (2018). Cirrus horizontal heterogeneity and 3-D radiative effects on cloud optical property retrievals from MODIS near to thermal infrared channels as a function of spatial resolution. *Journal of Geophysical Research: Atmospheres*, *123*(19), 11141–11153. https://doi.org/10.1029/2018JD028726

Gu, Y., & Liou, K. N. (2006). Cirrus cloud horizontal and vertical inhomogeneity effects in a GCM. *Meteorology and Atmospheric Physics*, *91*(1), 223–235. https://doi.org/10.1007/s00703-004-0099-2

Guttman, N. B., Hosking, J. R. M., & Wallis, J. R. (1993). Regional precipitation quantile values for the continental United States computed from L-moments. *Journal of Climate*, *6*(12), 2326–2340. https://doi.org/10.1175/1520-0442(1993)006<2326:rpqvft>2.0.co;2

Holton, J. R., Haynes, P. H., McIntyre, M. E., Douglass, A. R., Rood, R. B., & Pfister, L. (1995). Stratosphere-troposphere exchange. *Reviews of Geophysics*, *33*(4), 403–439. https://doi.org/10.1029/95RG02097

Hosking, J. R. M. (1990). L-moments: Analysis and estimation of distributions using linear combinations of order statistics. *Journal of the Royal Statistical Society: Series B*, *52*(1), 105–124. https://doi.org/10.1111/j.2517-6161.1990.tb01775.x

Jensen, E. J., Kärcher, B., Woods, S., Krämer, M., & Ueyama, R. (2024). The impact of gravity waves on the evolution of tropical anvil cirrus microphysical properties. *Journal of Geophysical Research: Atmospheres*, *129*(5), e2023JD039887. https://doi.org/10.1029/2023JD039887

Jensen, E. J., Pfister, L., Jordan, D. E., Bui, T. V., Ueyama, R., Singh, H. B., et al. (2017). The NASA airborne tropical tropopause experiment: High-altitude aircraft measurements in the tropical Western Pacific. https://doi.org/10.1175/BAMS-D-14-00263.1

Kanji, Z. A., Welti, A., Chou, C., Stetzer, O., & Lohmann, U. (2013). Laboratory studies of immersion and deposition mode ice nucleation of ozone aged mineral dust particles. *Atmospheric Chemistry and Physics*, *13*(17), 9097–9118. https://doi.org/10.5194/acp-13-9097-2013

Krämer, M., Rolf, C., Luebke, A., Afchine, A., Spelten, N., Costa, A., et al. (2016). A microphysics guide to cirrus clouds – Part 1: Cirrus types. *Atmospheric Chemistry and Physics*, *16*(5), 3463–3483. https://doi.org/10.5194/acp-16-3463-2016

Krämer, M., Rolf, C., Spelten, N., Afchine, A., Fahey, D., Jensen, E., et al. (2020a). Supplement of: A microphysics guide to cirrus – Part 2: Climatologies of clouds and humidity from observations. *Atmospheric Chemistry and Physics*, *20*(20), 12569–12608. https://doi.org/10.5194/acp-20-12569-2020-supplement

Krämer, M., Rolf, C., Spelten, N., Afchine, A., Fahey, D., Jensen, E., et al. (2020b). A microphysics guide to cirrus – Part 2: Climatologies of clouds and humidity from observations. *Atmospheric Chemistry and Physics*, *20*(21), 12569–12608. https://doi.org/10.5194/acp-20-12569-2020

Krämer, M., Spelten, N., Rolf, C., & Spang, R. (2025a). A microphysics guide to cirrus – Part 3: Occurrence patterns of cloud particles. *Atmospheric Chemistry and Physics*, *25*(20), 13563–13583. https://doi.org/10.5194/acp-25-13563-2025

Krämer, M., Spelten, N., Rolf, C., & Spang, R. (2025b). Cirrus guide III in-situ dataset [Dataset]. https://doi.org/10.34730/9EF25DADB84F4E7D9E0281CCB4086A3B

Liang, Q., Douglass, A. R., Duncan, B. N., Stolarski, R. S., & Witte, J. C. (2009). The governing processes and timescales of stratosphere-to-troposphere transport and its contribution to ozone in the Arctic troposphere. *Atmospheric Chemistry and Physics*, *9*(9), 3011–3025. https://doi.org/10.5194/acp-9-3011-2009

Pan, L. L., Atlas, E. L., Salawitch, R. J., Honomichl, S. B., Bresch, J. F., Randel, W. J., et al. (2017). The convective transport of active species in the tropics (CONTRAST) experiment. https://doi.org/10.1175/BAMS-D-14-00272.1

Pan, L. L., Bowman, K. P., Atlas, E. L., Wofsy, S. C., Zhang, F., Bresch, J. F., et al. (2010). The stratosphere–troposphere analyses of regional transport 2008 experiment. https://doi.org/10.1175/2009BAMS2865.1

Podglajen, A., Plougonven, R., Hertzog, A., & Jensen, E. (2018). Impact of gravity waves on the motion and distribution of atmospheric ice particles. *Atmospheric Chemistry and Physics*, *18*(14), 10799–10823. https://doi.org/10.5194/acp-18-10799-2018

Schäfer, M., Bierwirth, E., Ehrlich, A., Jäkel, E., Werner, F., & Wendisch, M. (2017). Directional, horizontal inhomogeneities of cloud optical thickness fields retrieved from ground-based and airborne spectral imaging. *Atmospheric Chemistry and Physics*, *17*(3), 2359–2372. https://doi.org/10.5194/acp-17-2359-2017

Voigt, C., Schumann, U., Minikin, A., Abdelmonem, A., Afchine, A., Borrmann, S., et al. (2017). ML-CIRRUS: The airborne experiment on natural cirrus and contrail cirrus with the high-altitude long-range research aircraft HALO. https://doi.org/10.1175/BAMS-D-15-00213.1

Wendisch, M., Pöschl, U., Andreae, M. O., Machado, L. A. T., Albrecht, R., Schlager, H., et al. (2016). ACRIDICON–CHUVA campaign: Studying tropical deep convective clouds and precipitation over Amazonia using the new German research aircraft HALO. https://doi.org/10.1175/BAMS-D-14-00255.1

Wolters, E. L. A., Deneke, H. M., van den Hurk, B. J. J. M., Meirink, J. F., & Roebeling, R. A. (2010). Broken and inhomogeneous cloud impact on satellite cloud particle effective radius and cloud-phase retrievals. *Journal of Geophysical Research*, *115*(D10). https://doi.org/10.1029/2009JD012205

Zhang, C., Zhang, Y., Wolf, M. J., Nichman, L., Shen, C., Onasch, T. B., et al. (2020). The effects of morphology, mobility size, and secondary organic aerosol (SOA) material coating on the ice nucleation activity of black carbon in the cirrus regime. *Atmospheric Chemistry and Physics*, *20*(22), 13957–13984. https://doi.org/10.5194/acp-20-13957-2020

Zhuravleva, T. B., & Nasrtdinov, I. M. (2021). Effect of microstructure and horizontal inhomogeneity of broken cirrus clouds on mean solar radiative fluxes in the visible wavelength region: Results of numerical simulation. *Atmospheric and Oceanic Optics*, *34*(6), 678–688. https://doi.org/10.1134/S1024856021060294

References From the Supporting Information

Thornberry, T. D., Rollins, A. W., Avery, M. A., Woods, S., Lawson, R. P., Bui, T. V., & Gao, R.-S. (2017). Ice water content-extinction relationships and effective diameter for TTL cirrus derived from in situ measurements during ATTREX 2014. *Journal of Geophysical Research: Atmospheres*, *122*(8), 4494–4507. https://doi.org/10.1002/2016JD025948